

Realization of Room-Temperature Phonon-limited Carrier Transport in Monolayer MoS₂ by Dielectric and Carrier Screening

Zhihao Yu, Zhun-Yong Ong, Yiming Pan, Yang Cui, Run Xin, Yi Shi, Baigeng Wang, Yun Wu, Tangsheng Che⁴, Yong-Wei Zhang, Gang Zhang* & Xinran Wang**

Zhihao Yu, Yang Cui, Run Xin, Prof. Yi Shi, Prof. Xinran Wang
National Laboratory of Solid State Microstructures, School of Electronic Science and Engineering, and Collaborative Innovation Center of Advanced Microstructures
Nanjing University, Nanjing 210093, P. R. China

E-mail: xrwang@nju.edu.cn, yshi@nju.edu.cn

Zhun-Yong Ong, Yong-Wei Zhang, Gang Zhang

Institute of High Performance Computing, 1 Fusionopolis Way, 138632, Singapore

E-mail: zhangg@ihpc.a-star.edu.sg

Yiming Pan, Prof. Baigeng Wang

National Laboratory of Solid State Microstructures, School of Physics, Nanjing University, Nanjing 210093, P. R. China

Yun Wu, Tangsheng Chen

Science and Technology on Monolithic Integrated Circuits and Modules Laboratory, Nanjing Electronic Device Institute, Nanjing, China

Keywords: molybdenum disulfide (MoS₂), phonon-transport, mobility, interface

Research into the physical properties of MoS₂ and other semiconducting transition metal dichalcogenides^[1] (TMDs) has increased considerably in recent years, owing to their potential applications in post-CMOS electronics^[2-4], optoelectronics^[5-7] and valleytronics^[8-10]. Some of the properties of monolayer MoS₂ that are advantageous for electronic applications include a direct band gap of 1.8 eV^[11,12] as well as a film thickness of less than 1 nm which gives superior electrostatic control of the charge density and current even at the transistor scaling limit^[3,13]. In spite of these favorable properties, the widely reported low electron mobility in monolayer MoS₂ poses a serious obstacle to its integration into post-CMOS nanoelectronics. The nature

of charge transport in MoS₂, especially at room temperature, remains poorly understood despite considerable amount of theoretical and experimental researches. For example, the theoretically predicted intrinsic phonon-limited mobility at room temperature is in the range of 200-410 cm²/Vs^[14,15] while most experimentally reported values are much smaller^[16-23]. Before any semiconducting material can become useful for potential nanoelectronic device applications, a critical assessment of its intrinsic charge transport properties at room temperature is needed, requiring the realization of high-quality samples with carrier mobility in the phonon-limited regime. The phonon-limited transport regime was demonstrated for graphene^[24] and carbon nanotubes^[25]. However, despite many recent efforts to improve carrier mobility by means of topgate^[17], chemical functionalization^[21] and BN gate dielectrics^[22], phonon-limited transport regime has not been explicitly demonstrated in monolayer TMDs including MoS₂.

The possible reasons for the discrepancy between the theoretical upper limit and experimental data include Coulomb impurities (CI), traps and defects in low-quality samples^[19-23]. These extrinsic sources of scattering have so far precluded any rigorous examination of the intrinsic scattering mechanisms that affect electron mobility. A particularly important source of scattering is from CI at the semiconductor-dielectric interface, which is believed to be the most important limiting factor in current MoS₂ devices^[26]. Recently, it has been demonstrated that by sandwiching the monolayer MoS₂ channel between BN layers, CI scattering can be significantly suppressed, leading to a record-high mobility of over 1000 cm²/Vs at low temperatures^[22-23]. The technologically relevant room-temperature mobility, however, still lags the best devices on SiO₂ for reasons not well understood. Nonetheless, significant recent progress in reducing the deleterious effects of CI, traps and defects on the

mobility^[20-23] begin to set the stage for the realization of room-temperature charge transport in the phonon-limited regime.

It has been shown experimentally that the deposition of a high- κ top oxide can increase the mobility of MoS₂ through the purported reduction of CI scattering^[17,27,28]. However, another significant, yet often overlooked, factor in the mobility improvement is the high carrier density that can be accessed experimentally in such dual-gated device configurations. In addition, the remote interaction between the electrons and the substrate surface optical (SO) phonons plays a crucial role in limiting charge transport in atomically thin crystals adjacent to high- κ dielectrics^[24,29]. Therefore, determining quantitatively the contribution from the various scattering processes to the resistivity poses an enormous challenge that warrants a synergy between an experimental study of the electron mobility with precisely controlled device parameters (including carrier density n , dielectric constant ϵ , density of CI n_{CI} , temperature T) and numerical modeling to interpret the mobility dependence on these parameters in terms of the underlying scattering mechanisms.

In this Communication, we perform a combined experimental and theoretical study of the electron transport in high-quality, thiol-treated monolayer MoS₂ supported on different substrates (SiO₂, HfO₂ or Al₂O₃). By suppressing the effects of CI scattering through dielectric and carrier screening, we are able to fabricate monolayer MoS₂ transistors with a room-temperature mobility of ~ 150 cm²/Vs, which is among the highest room-temperature mobility for monolayer MoS₂ devices^[17,22,23]. Given the excellent sample quality and simple device structure, we can extract quantitatively the contributions from CI, intrinsic and remote phonons. Our analysis confirms that the mobility in these devices is limited by intrinsic and remote phonons rather than CI at room temperature.

Before we report our mobility results, we first give an overview of the physics underlying the scattering of electrons by sources in the substrate. In supported MoS₂, the electrons experience random static and time-dependent electric fields at the semiconductor-dielectric interface. These fields are physically created by the CI as well as by the dipoles of the oscillating metal-oxide bonds originating from the polar optical phonons in the dielectric. Therefore, in addition to scattering from the intrinsic acoustic and optical phonons, the interaction between the electrons and these fields introduces another two processes that limit electron mobility: (1) elastic scattering with the CI which are presumably located at the surface of the substrate, and (2) the remote interaction with the SO phonons.

The interaction between the electrons and the CI in the MoS₂ can be described by the term $H_{CI} = \sum_{k,q} \rho_{CI}(q) \phi_q^{scr} c_{k+q}^\dagger c_k$ where $\rho_{CI}(q)$ and ϕ_q^{scr} are the Fourier transforms of the CI distribution and the screened potential, respectively, and c_k^\dagger (c_k) is the electron creation (annihilation) operator. We drop the valley and spin indices to simplify the discussion. The screened potential can be expressed as

$\phi_q^{scr} = \frac{\phi_q}{\varepsilon_{2D}(q,T)}$, where $\phi_q = \frac{e^2}{(\varepsilon_{box} + \varepsilon_0)q}$ is the bare potential and e is the electron charge; ε_{box} and ε_0 are in turn the static permittivity of the substrate and vacuum.

The screening of the bare CI by the substrate and the free electrons is described by the

generalized screening function^[30,31] $\varepsilon_{2D}(q,T) = 1 + \frac{2\varepsilon_{el}(q)}{\varepsilon_{box} + \varepsilon_0}$, where $\varepsilon_{el}(q)$

corresponds to the electronic part of the dielectric function and depends on the carrier density n . As n increases, screening becomes stronger, reducing the scattering potential and increasing the CI-limited mobility.

To illustrate the effect of screening, we plot in Fig. 1a the real space potential profile for a point CI in MoS₂ under four different scenarios. We observe a reduction in the size of the potential profile when there is polarization charge screening. The effective size of the CI also depends on the substrate dielectric constant which directly reduces the bare potential as well as indirectly weakens polarization charge screening. Therefore, a combination of high κ and high carrier density is most effective in reducing the effective size of the CI, as shown in the lower right panel of Fig. 1a. However, on the HfO₂ substrate, despite the large increase in carrier density, the reduction in the profile is not substantial. This is because a high permittivity weakens all Coulomb interactions, including screening.

The variation in κ and n also affects the CI-limited mobility μ_{CI} . Figure 1b shows the simulated μ_{CI} for the SiO₂ substrate over $T = 10\text{-}400$ K and $n = 0.1\text{-}10 \times 10^{12}$ cm⁻² with $n_{CI} = 1 \times 10^{12}$ cm⁻². The μ_{CI} increases monotonically with n because screening of CI becomes more effective at higher carrier density. Given that CI scattering is the dominant scattering mechanism in most MoS₂ samples, this indicates that the experimental mobility should be measured over a wide range of n before a meaningful comparison can be made with numerical models and that a higher carrier density is required to reach greater mobility. A less intuitive result is the decrease in μ_{CI} as a function of T , which is due to the weakening of the charge polarizability at higher temperatures and is often interpreted mistakenly as a signature of phonon-limited charge transport. This μ_{CI} decrease has also been shown to be proportionally smaller for a high- κ substrate^[30]. Fig. 1c shows the simulated room temperature μ_{CI} at experimentally accessible $n = 3 \times 10^{12}$, 7×10^{12} , 1.1×10^{13} and 1.5×10^{13} cm⁻² as a function of κ . Generally, μ_{CI} increases with κ because the higher permittivity reduces the effective charge on the CI and hence the scattering rate. For $\kappa = 40$, μ_{CI} can be as

high as $\sim 1100 \text{ cm}^2/\text{Vs}$ at room temperature. However, the extent μ_{CI} increases with κ is proportionally smaller at high n because the greater screening by the polarization charge diminishes the screening by the substrate (Fig. 1d).

The other major external process that affects the electron mobility is its remote interaction with the substrate SO phonons, described by the term

$$H_{SO} = \sum_{k,q} M_q c_{k+q}^\dagger c_k (a_q + a_{-q}) \quad \text{where } M_q \text{ is the coupling coefficient and } a_q^\dagger \text{ (} a_q \text{)}$$

is the phonon creation (annihilation) operator. For a highly polar oxide like HfO_2 , the coupling coefficient is especially strong because of the large difference between the optical and static dielectric responses. The strength of the bare coupling coefficient

can be quantified by the dimensionless coupling constant^[32]

$$\alpha_{SO} = \frac{e^2}{8\pi\hbar} \left(\frac{m^*}{2\hbar\omega_{SO}} \right)^{1/2} \left(\frac{1}{\epsilon_{SO}^\infty} - \frac{1}{\epsilon_{SO}^0} \right), \quad \text{where } \epsilon_{SO}^\infty \text{ and } \epsilon_{SO}^0 \text{ are the optical and static}$$

dielectric response of the interface, respectively. α_{SO} is analogous to the

dimensionless Froehlich coupling constant usually defined for polarons in bulk polar

insulators and is given in Table 1. Generally, α_{SO} is larger for strongly polar

(high- κ) dielectrics such as HfO_2 and shares the same physical origin as the high

permittivity of the dielectric. In a highly polar insulator, the bonds can be polarized

more easily in response to an external electric field and screen a CI more effectively.

However, the large polarization from the oscillating metal-oxide bond in the dielectric

also couples the associated lattice vibration (phonon) more strongly to free carriers at

the surface^[33]. As expected, HfO_2 (SiO_2) has the largest (smallest) average α_{SO} of

the three oxides studied in this work and the strongest (weakest) remote phonon

scattering as well as the lowest (highest) SO phonon-limited mobility μ_{SO} , shown in

Fig. S2. In our semi-classical charge transport model, CI- and SO-phonon scattering

are included along with other intrinsic phonon scattering processes. The detailed calculation of mobility is described in Supplementary Information.

The experimental data are obtained from field effect transistors fabricated on high-quality MoS₂ samples which we recently developed using thiol chemistry to improve the sample and interface quality²¹. The room-temperature mobility for backgated devices on SiO₂, which was limited by CI scattering, could be as high as 80 cm²/Vs. Here we use the same thiol treatment on monolayer MoS₂ samples mechanically exfoliated on 10nm high-κ oxide/285nm SiO₂/Si substrates (Fig. 2a inset, detailed device fabrication process is described in Supplementary Information). Compared to bare SiO₂/Si substrates, the addition of a thin layer of high-κ oxide only changes the gate capacitance C_g by less than 1%, but yields a 50% increase in carrier density by sustaining a much higher (~150V) backgate voltage V_g. The dielectric constant of HfO₂ and Al₂O₃ used in this work are ~16.5 and 10 respectively obtained from standard capacitance measurements (see Supplementary Information). Compared to the topgate devices, our devices are free from the impurities and contaminations introduced in the topgate fabrication^[34,35], and much easier to model quantitatively.

Fig. 2a shows variable-temperature measurements of four-probe conductivity σ as a function of V_g for a representative device on HfO₂ (H1). The curves all intersect near V_g≈70V (corresponding to $n=C_g V_g \approx 5.0 \times 10^{12} \text{cm}^{-2}$), a signature of metal-insulator transition (MIT) due to charge traps at the interface²¹. Since the effect of traps is dominant at low carrier density (comparable or lower than the critical density of MIT) and low temperature²¹, we focus our discussion on the opposite limit ($n > 7 \times 10^{12} \text{cm}^{-2}$) in order to unambiguously model CI and phonon scattering without being complicated

$$\mu(n,T) = \frac{d\sigma(n,T)}{C_g dV_g}$$

by traps. Fig. 2b shows the four-probe field-effect mobility as a function of temperature for three representative devices on HfO₂, Al₂O₃ and SiO₂ respectively (H1, A2 and S1). For fair comparison, μ is extracted at $n=7.1 \times 10^{12} \text{cm}^{-2}$ for all three devices. We clearly observe that μ increases with the dielectric constant of the oxides. The solid lines in Fig. 2b are best theoretical fits at high temperatures taking into account intrinsic and SO phonons and CI. The extracted n_{CI} is similar for all three oxide substrates (Table 1), which is not surprising considering that the oxides have similar roughness (Fig. S3) and are subjected to the same thiol treatment prior to exfoliation of MoS₂. However, process variations could cause a fluctuation in n_{CI} of up to ~50%. Since HfO₂ (SiO₂) has the highest (lowest) average α_{so} among the three oxides (Table 1), the observed trend in mobility suggests that CI scattering in HfO₂ (SiO₂) is the weakest (strongest). Indeed, our modeling shows that μ_{CI} at room temperature increases by 270% when switching SiO₂ to HfO₂ with similar $n_{CI} \sim 0.9 \times 10^{12} \text{cm}^{-2}$ (Table 1). This is the first clear demonstration of the dielectric screening effect under well-controlled conditions, unlike in dual-gated devices where CI density is likely increased by the fabrication process and no rigorous comparison can be made with single-gated devices.

Fig. 2c and Fig. S5 depict the temperature dependence of mobility at $n=10.5 \times 10^{12} \text{cm}^{-2}$ for several devices on HfO₂ and Al₂O₃ respectively. Excellent agreement between experiment (symbols) and modeling (solid lines) is achieved through the whole temperature range of 20-300K, reassuring the accuracy of our model. The device H1 (A2), which is the best device on HfO₂ (Al₂O₃), shows a room-temperature mobility of 148cm²/Vs (113cm²/Vs), an 85% (41%) improvement over similar samples on SiO₂²¹. The mobility at 20K of 847cm²/Vs (591cm²/Vs)

shows an even more dramatic improvement. These improvements result primarily from dielectric and carrier screening effects. Using the fitting parameters in Table 1, the contribution of CI and phonons can be quantitatively calculated (dashed and dotted lines Fig. 2c). We find that the lines cross at $T=233\text{K}$ ($T=275\text{K}$) for device H1 (H2), which means that above that temperature, these devices are no longer limited by CI scattering, but by phonons. For device H1, the room-temperature μ_{CI} and phonon-limited mobility $[\mu_{ph}^{-1} + \mu_{so}^{-1}]^{-1}$ are $372\text{cm}^2/\text{Vs}$ and $215\text{cm}^2/\text{Vs}$ respectively. This is the first time that phonon-limited transport regime has been explicitly demonstrated for any monolayer TMDs. However, for devices on Al_2O_3 , transport is still limited by CI in the measured temperature range due to reduced dielectric screening (Fig. S5b). Furthermore, we find that the experimentally extracted μ_{CI} can be well fitted by T^γ for $T>100\text{K}$, where $\gamma=0.4$ and 0.8 for H1 and A2, respectively (Fig. S6b). The power-law dependence of μ_{CI} is in good agreement with theoretical simulations (Fig. S6a), further supporting our analysis. The smaller γ for HfO_2 is attributed to more significant effect of dielectric screening induced by higher dielectric constant.

Recently, it was suggested theoretically that high- κ dielectrics are not ideal substrates for ultra-clean MoS_2 because of remote phonon scattering²⁶. Our calculation concurs with this proposition. Ultimately, the effective dielectric screening in a high- κ dielectric shares the same physical origins as the strong remote phonon coupling (α_{so}): both are due to the large ionic polarizability of the metal-oxide bond. When the density of CI is reduced, low- κ dielectrics with less polar nature (such as BN and SiO_2) will be advantageous. Fig. 2d plots the calculated room-temperature mobility as a function of n_{CI} for the three oxides studied in this work, along with our experimental data. Two regimes emerge in the diagram. At high CI density, the

mobility is limited by CI scattering, thus HfO₂ is the best among the three oxides due to dielectric screening. A $1/n_{CI}$ scaling is observed in the limit of very strong impurity, where the mobility is generally below 100cm²/Vs. Most experimental results to date fall in this regime¹⁶⁻²³. At low CI density, the mobility is limited by phonons and is nearly independent of n_{CI} . In this regime, HfO₂ is outperformed by the other two oxides. If n_{CI} can be reduced below $\sim 0.3 \times 10^{12}$ cm⁻² (which is roughly the crossover point between the two regimes), the use of low- κ dielectrics such as SiO₂ and BN would be favorable. In this case, one would expect a room-temperature mobility of over 200 cm²/Vs for monolayer MoS₂.

Let us now discuss another important aspect of screening by charge carriers, which is manifested experimentally in the carrier-density-dependent mobility. In Fig. 3a we plot the mobility of device H1 under $n=10.5 \times 10^{12}$, 8.5×10^{12} and 7.1×10^{12} cm⁻², in line with the modeling results using the parameters in Table 1 (solid lines). The contribution from phonons (blue shaded region) and CI (yellow shaded region) are plotted separately. The monotonic increase of μ with n is due to the screening effect of both μ_{CI} and μ_{SO} . After subtracting the contribution of phonons, we find that μ_{CI} has a linear relationship with n for all the devices (Fig. 3b). This is because at high temperatures, the polarization charge is diluted so that screening is significantly weaker and the scattering cross section of the CI is similar to that of the bare CI, especially when the substrate κ is high. For a 2D electron gas with a parabolic dispersion, it is known that scattering with a bare Coulomb potential leads to a mobility proportional to n .^[36] In Fig. 3b, the mobility value and the linear coefficient vary among devices due to different n_{CI} and κ . The variations of n_{CI} can be normalized by $\sigma_{CI} \equiv en_{CI}\mu_{CI}$, which has a unit of conductivity (Fig. 3b inset). After the normalization, devices on the same high- κ substrate collapse onto the same curve,

well described by our modeling (lines in Fig. 3b inset). The curve for HfO₂ is higher than the one for Al₂O₃ because the former's larger dielectric constant reduces the effective charge on its CI, resulting in a proportionally smaller scattering cross section. This consistency provides further evidence that we have accurately differentiated the CI contribution to the resistivity from the phonon contribution.

Another reason for the improved mobility is the screening-induced reduction in remote phonon scattering and μ_{SO} (Fig. 3a, dotted lines). Recall that the SO phonons are associated with the oscillating polarized metal-oxide bonds in the dielectric. However, the large polarization of the bond also couples the SO phonon to the surface²¹ charge from the MoS₂, giving rise to screening of the electron-phonon coupling and a smaller contribution to the resistivity.

In conclusion, by systematic engineering of the material quality, dielectric environment and carrier density, we are able to achieve room-temperature phonon-limited transport in monolayer MoS₂ for the first time by screening of CI scattering. Through rigorous theoretical modeling, we identify CI and remote phonons as the key limitations in current MoS₂ devices. Our model indicates that there is limited room for further mobility improvement on HfO₂ ($\mu < 215 \text{ cm}^2/\text{Vs}$) if we are constrained by the possibility of dielectric breakdown to a maximum carrier density of $1 \times 10^{13} \text{ cm}^{-2}$. The present methodology of combining high-k dielectric screening and interface functionalization is a generic route to increase carrier mobility in other TMDs such as WS₂ (Ref. 37). Future improvement of the mobility in TMDs requires continued interface engineering that combines a low CI density and weak remote phonon scattering simultaneously.

Supporting Information

Supporting Information is available from the Wiley Online Library or from the author.

Acknowledgements

Z. H. Yu, Z. Y. Ong, Y. M. Pan contributed equally to this work. This work was supported in part by National Key Basic Research Program of China 2013CBA01604, 2015CB921600; National Natural Science Foundation of China 61325020, 61261160499, 11274154, 61521001; MICM Laboratory Foundation 9140C140105140C14070; a project funded by the Priority Academic Program Development of Jiangsu Higher Education Institutions; “Jiangsu Shuangchuang” program and ‘Jiangsu Shuangchuang Team’ Program.

Received: ((will be filled in by the editorial staff))

Revised: ((will be filled in by the editorial staff))

Published online: ((will be filled in by the editorial staff))

- [1] A. D. Yoffe, *Annu. Rev. Mater. Sci.*, **1973**, 3, 147.
- [2] Q. H. Wang, K. Kalantar-Zadeh, A. Kis, J. N. Coleman, & M. S. Strano. *Nature Nanotech.*, **2012**, 7, 699.
- [3] G. Fiori, F. Bonaccorso, G. Iannaccone, T. Palacios, D. Neumaier, A. Seabaugh, S. K. Banerjee, L. Colombo. *Nature Nanotech.*, **2014**, 9, 768.
- [4] D. Lembke, S. Bertolazzi, & A. Kis, *Acc. Chem. Res.* **2015**, 48 100.
- [5] J. S. Ross, P. Klement, A. M. Jones, N. J. Ghimire, J. Q. Yan, D. G. Mandrus, T. Taniguchi, K. Watanabe, K. Kitamura, W. Yao. *Nature Nanotech.*, **2014**, 9, 268.
- [6] W. J. Yu, Y. Liu, H. L. Zhou, A. X. Yin, Z. Li, Y. Huang, X. F. Duan. *Nature Nanotech.*, **2013**, 8, 952.
- [7] F. H. L. Koppens, T. Mueller, P. Avouris, A. C. Ferrari, M. S. Vitiello, & M. Polini. *Nature Nanotech.*, **2014**, 9, 780
- [8] D. Xiao, G. B. Liu, W. Feng, X. Xu, & W. Yao, *Phys. Rev. Lett.*, **2012**, 108,

196802.

- [9] H. Zeng, J. Dai, W. Yao, D. Xiao, & X. Cui, *Nature Nanotech.*, **2012**, **7**, 490
- [10] A. M. Jones, H. Yu, N. J. Ghimire, S. Wu, G. Aivazian, J. S. Ross, & X. Xu, *Nature Nanotech.*, **2013**, **8**, 634
- [11] K. F. Mak, C. Lee, J. Hone, J. Shan, J., & T. F. Heinz, *Phys. Rev. Lett.*, **2010**, **105**, 136805
- [12] A. Splendiani, L. Sun †, Y. B. Zhang, T. S. Li, J. Kim, C. Y. Chim, G. Galli and F. Wang, *Nano Lett.*, **2010**, **10**, 1271
- [13] L. Liu, S. Bala Kumar, Y. Ouyang, & J. Guo, *IEEE Trans. Electron Devices*, **2011**, **58** 3042
- [14] X. Li, J. T. Mullen, Z. Jin, K. M. Borysenko, M. B. Nardelli, & K. W. Kim, *Phys. Rev. B*, **2013**, **87**, 115418
- [15] K. Kaasbjerg, K. S. Thygesen, K. W. Jacobsen. *Phys. Rev. B*, **2012**, **85**, 115317.
- [16] H. Schmidt, S. F. Wang, L. Q. Chu, M. Toh, R. Kumar, W. J. Zhao, A. H. Castro Neto, J. Martin, S. Adam, B. Özyilmaz, and G. Eda. *Nano Lett*, **2014**, **14**, 1909.
- [17] B. Radisavljevic, & A. Kis, *Nature Mater.*, **2013**, **12**, 815
- [18] H. Liu, M. Si, S. Najmaei, A. T. Neal, Y. C. Du, P. M. Ajayan, J. Lou, and P. D. Ye, *Nano Lett.*, **2013**, **13**, 2640.
- [19] B. W. Baugher, H. O. Churchill, Y. Yang, & P. Jarillo-Herrero, *Nano Lett.*, **2013**, **13** 4212.
- [20] H. Qiu, T. Xu, Z. L. Wang, Ren. W, H. Y. Nan, Z. H. Ni, Q. Chen, S. J. Yuan, F. Miao, F. Q. Song, G. Long, Y. Shi, L. T. Sun, J. L. Wang. X. R. Wang. *Nature*

Commun, **2013**, 4, 2642.

- [21] Z. H. Yu, Y. M. Pan, Y. T. Shen, Z. L. Wang, Z. Y. Ong, T. Xu, R. Xin, L. J. Pan, B. G. Wang, L. T. Sun, J. L. Wang, G. Zhang, Y. W. Zhang, Y. Shi, X. R. Wang. *Nature Commun*, **2014**, 5, 5290.
- [22] X. Cui, G. H. Lee, Y. D. Kim, G. Arefe, P. Y. Huang, C. H. Lee, D. A. Chenet, X. Zhang, L. Wang, F. Ye, F. Pizzocchero, B. S. Jessen, K. Watanabe, T. Taniguchi, D. A. Muller, T. Low, P. Kim and J. Hone, *Nature Nanotech.* **2015**, 10, 534
- [23] Y. Liu, H. Wu, H. C. Cheng, S. Yang, E. Zhu, Q. Y. He, M. Ding, D. Li, J. Guo, N. Weiss, Y. Huang, X. Duan, *Nano Lett.*, **2015**, 15, 3030
- [24] L. Wang, I. Meric, P. Y. Huang, Q. Gao, Y. Gao, H. Tran, T. Taniguchi, K. Watanabe, L. M. Campos, D. A. Muller, J. Guo, P. Kim, J. Hone, K. L. Shepard, C. R. Dean *Science*, **2013**, 342, 614
- [25] E. Pop, D. Mann, J. Cao, Q. Wang, K. Goodson, & H. Dai, *Phys. Rev. Lett.*, **2005**, 5, 155505.
- [26] N. Ma, D. Jena. *Phys. Rev. X*, **2014**, 4, 011043.
- [27] B. Radisavljevic, A. Radenovic, J. Brivio, V. Giacometti, & A. Kis, *Nature Nanotech.*, **2011**, 6, 147
- [28] M. Amani, M. L. Chin, A. Glen Birdwell, T. P. O'Regan, S. Najmaei, Z. Liu³, P. M. Ajayan, J. Lou and M. Dubey *Appl. Phys. Lett.*, **2013**, 102, 193107
- [29] K. Zou, X. Hong, D. Keefer, J. Zhu. *Phys. Rev. Lett*, **2010**, 105, 126601..
- [30] Z. Y. Ong, V. M. Fischetti. *Phys. Rev. B*, **2013**, 88, 165316.
- [31] P. F. Maldague. *Surf. Sci*, **1978**, 73, 296..

- [32] M. V. Fischetti, D. A. Neumayer, E. A. Cartier. *Appl. Phys.*, **2001**, 90, 4587.
- [33] S. Q. Wang, G. D. Mahan. *Phys. Rev. B*, **1972**, 6, 4517..
- [34] Z. Wang, Z. Zhang, H. Xu, L. Ding, S. Wang, & L. M. Peng, *Appl. Phys. Lett.*, **2010**, 96, 173104
- [35] J. B. Oostinga, H. B. Heersche, X. Liu, A. F. Morpurgo, & L. M. Vandersypen, *Nature Mater.*, **2008**, 7, 151
- [36] E. H. Hwang, & S. D. Sarma, *Phys. Rev. B*, **2009**, 79, 165404.
- [37] Y. Cui, R. Xin, Z. H. Yu, Y. M. Pan, Z. Y. Ong, X. X. Wei, J. Z. Wang, H. Y. Nan, Z. H. Ni, Y. Wu, T. S. Chen, Y. Shi, B. G. Wang, G. Zhang, Y. W. Zhang, X. R. Wang, *Adv. Mater.* in press. **2015**.

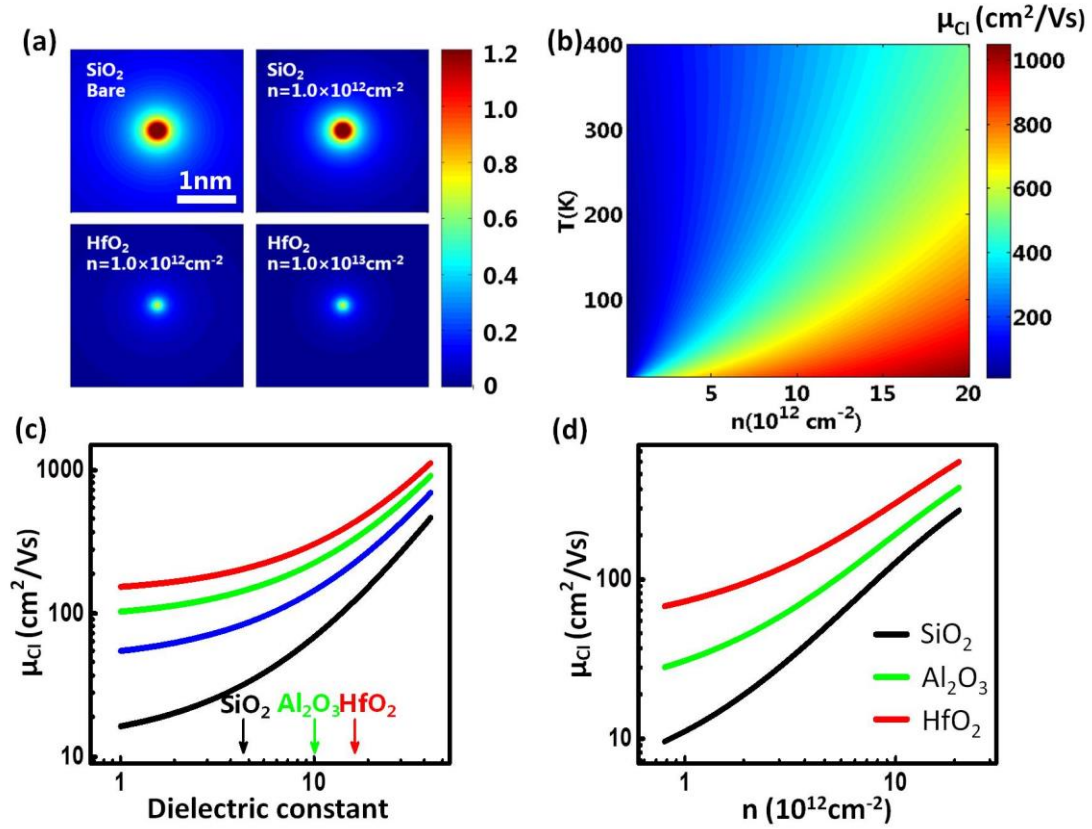


Figure 1. Modeling of charged impurity scattering in monolayer MoS₂. (a) The real space distribution of screened Coulomb potential for a point charge in MoS₂ on SiO₂ ($\kappa = 3.9$, upper panels) and HfO₂ ($\kappa = 16.5$, lower panels) at different carrier densities. (b) μ_{CI} as a function of carrier density and temperature on HfO₂ substrate ($n_{CI} = 1.0 \times 10^{12} \text{ cm}^{-2}$). (c) μ_{CI} as a function of dielectric constant at different carrier density ($T = 300 \text{ K}$). From top to bottom, $n = 1.5 \times 10^{13} \text{ cm}^{-2}$ (red), $1.1 \times 10^{13} \text{ cm}^{-2}$ (green), $7.0 \times 10^{12} \text{ cm}^{-2}$ (blue) and $3.0 \times 10^{12} \text{ cm}^{-2}$ (black) respectively. (d) μ_{CI} as a function of carrier density on SiO₂ (black), Al₂O₃ (green) and HfO₂ (red) substrates ($T = 300 \text{ K}$, $n_{CI} = 1.0 \times 10^{12} \text{ cm}^{-2}$).

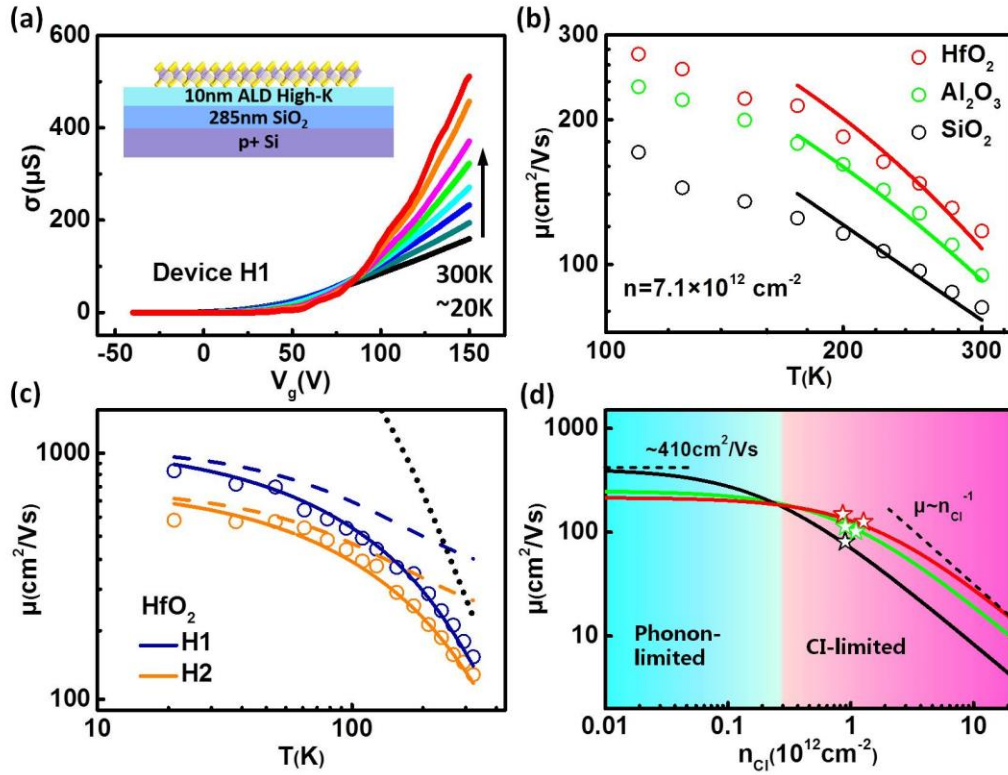


Figure 2. Effect of dielectric screening on the charge transport of monolayer

MoS₂. (a) Four-probe conductivity as a function of V_g for a representative device on

HfO₂ substrate (device H1). Inset shows a cartoon illustration of the device structure.

(b) Field-effect mobility as a function of temperature for three devices on SiO₂ (black),

Al₂O₃ (green) and HfO₂ (red) respectively, under $n=7.1 \times 10^{12} \text{ cm}^{-2}$ (symbols). Solid

lines are the modeling results at high temperature. (c) Field-effect mobility as a

function of temperature for two devices on HfO₂ substrate under $n=10.5 \times 10^{12} \text{ cm}^{-2}$

(symbols), together with the best theoretical fittings (solid lines, see Table 1 for fitting

parameters), the calculated CI-limited mobility (dashed lines), and the calculated

phonon-limited mobility (black dotted line). (d) Predicted field-effect mobility as a

function of n_{CI} for devices on SiO₂ (black line), Al₂O₃ (green line) and HfO₂ (red line)

substrate. The symbols are experimentally extrapolated data from five different devices (the parameters are listed in Table 1).

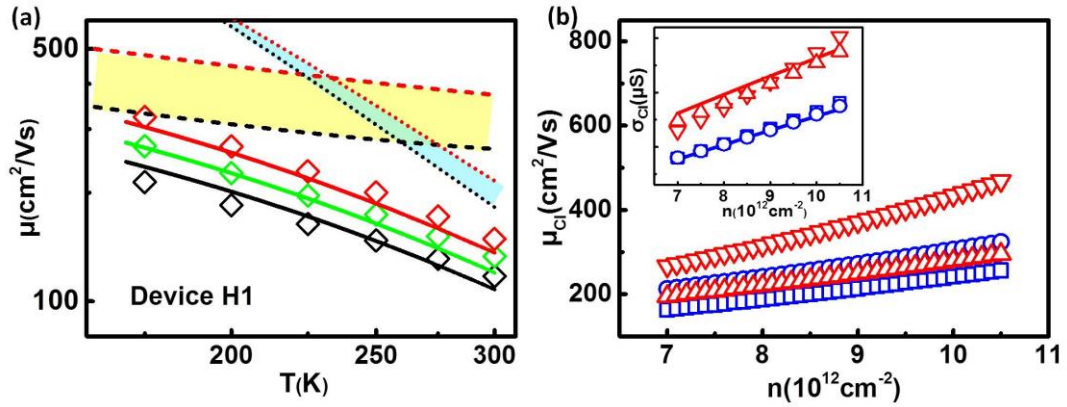


Figure 3. Effect of carrier screening on the charge transport of monolayer MoS₂.

(a) Field-effect mobility as a function of temperature under different carrier densities for device H1 on HfO₂ (symbols), together with the theoretical fittings (solid lines, see Table 1 for fitting parameters). From top to bottom, $n=10.5 \times 10^{13}$ cm⁻² (red), 8.5×10^{12} cm⁻² (green) and 7.1×10^{12} cm⁻² (black) respectively. The calculated CI-limited mobility and phonon-limited mobility in the same carrier density regime are denoted by the yellow and blue shaded area respectively. (b) CI-limited mobility as a function of carrier density for the four devices on Al₂O₃ and HfO₂ at $T=200$ K. Red up triangles: device H1; red down triangles: device H2; blue squares: device A1; blue circles: device A2. Inset is the normalized conductivity σ_{CI} as a function of carrier density for the four devices. Solid lines are modeling results using the parameters in Table 1.

Oxide	ϵ	ϵ^{∞}	α_{SO1}	α_{SO2}	ω_{TO1} (meV)	ω_{TO2} (meV)	ω_{LO1} (meV)	ω_{LO2} (meV)	ω_{SO1} (meV)	ω_{SO2} (meV)	Device #	n_{Cl} (cm ⁻²)	μ_{Cl} (300K) (cm ² /Vs)	μ (300K) (cm ² /Vs)
HfO ₂	16.5	4.23	1.27	-	40.0	-	79.0	-	73.2	-	H1	0.86×10 ¹²	372	148
											H2	1.27×10 ¹²	252	125
Al ₂ O ₃	10	2.56	0.18	1.32	48.2	71.4	56.5	120.4	56.0	108.0	A1	1.1×10 ¹²	164	101
											A2	0.85×10 ¹²	246	113
SiO ₂	3.9	2.5	0.41	0.28	55.6	138.1	62.6	153.3	61.0	149.0	S1	0.9×10 ¹²	101	81

Table 1 The mobility values and fitting parameters of the devices presented in this work are taken and derived from Refs. 27, 29 and 31.

Supplementary Information

1. Details of theoretical calculations
2. Growth and characterizations of high- κ oxides
3. Sample preparation, device fabrication and electrical measurements
4. Additional electrical data of devices on Al₂O₃ and HfO₂ substrate

1. Details of theoretical calculations

To analyze the electron mobility in monolayer MoS₂, we use a semiclassical model based on the relaxation time approximation. The electrons are assumed to move diffusively in the MoS₂ sheet, with an effective mass¹ of $m^* = 0.48m_0$ where m_0 is the free electron mass. However, their mobility is limited by scattering processes intrinsic and extrinsic to MoS₂. The expression for the electron mobility is given by^{2,3}

$$\mu = \frac{2e}{\pi n \hbar^2 k_B T} \int_0^\infty f(E)[1-f(E)]\Gamma(E)^{-1} E dE \quad (S1)$$

where e , n , \hbar , k_B and T are the electron charge quantum, the electron density, the Planck constant divided by 2π , the Boltzmann constant and the temperature, respectively.

The functions $f(E)$ and $\Gamma(E)$ in turn represent the Fermi-Dirac distribution and the momentum relaxation rate. The total electron mobility is computed using Matthiesen's rule²:

$\mu = (\mu_{CI}^{-1} + \mu_{ph}^{-1} + \mu_{SO}^{-1})^{-1}$ where μ_{CI} , μ_{ph} and μ_{SO} are the individual mobilities limited by scattering with CI, intrinsic phonons or SO phonons, respectively, and calculated using Eq. (S1) with the scattering rates Γ_{CI} (Coulomb impurities), Γ_{ph} (intrinsic phonons) or Γ_{SO} (surface optical phonons). The details of how the scattering rates are given in the following discussions.

a. Coulomb impurities

Coulomb impurity scattering is due to the charge centers near the oxide surface and also to sulfur vacancies within the MoS₂, and is known to be a major source of resistance to electron conduction in 2D crystals. It was shown by Ong and Fischetti³ that CI-limited charge

transport can have an electron mobility temperature dependence that is similar to that in phonon-limited charge transport.

The screened potential can be expressed as $\phi_q^{scr} = \frac{\phi_q}{\epsilon_{2D}(q,T)}$, where $\phi_q = \frac{e^2}{(\epsilon_{box}^0 + \epsilon_0)q}$ is the bare potential; ϵ_{box}^0 and ϵ_0 are in turn the static permittivity of the substrate and vacuum. The screening of the bare CI by the substrate and the free electrons is described by the generalized screening function $\epsilon_{2D}(q,T) = 1 + \frac{2\epsilon_{el}(q)}{\epsilon_{box}^0 + \epsilon_0}$, where $\epsilon_{el}(q) = -\frac{e^2}{2q}\Pi(q,T,E_F)$ corresponds to the electronic part of the dielectric function. $\Pi(q,T,E_F)$ is the temperature- and carrier density-dependent static polarizability, and represents the polarization charge screening of the CI. The exact form of $\Pi(q,T,E_F)$ is given in Refs. 3-5.

The CI scattering rate is³

$$\Gamma_{CI}(E_k) = \frac{n_{CI}}{2\pi\hbar} \int dk |\phi_{|k-k'|}^{scr}|^2 (1 - \cos\theta_{kk'}) \delta(E_k - E_{k'}), \quad (S2)$$

b. where $\theta_{kk'}$ is the scattering angle between the k and k' states and E_k is the energy. Thus, the CI-limited mobility μ_{CI} can be calculated using Eqs. (S1) and

(S2). Intrinsic phonon scattering

In our model, the intrinsic phonon scattering rate (Γ_{ph}) is due to electrons scattering with the longitudinal (LA) and transverse acoustic (TA), the intravalley polar longitudinal optical (Froehlich), the intervalley polar longitudinal optical (LO) and the intravalley homopolar optical (HP) phonons. Thus, we have $\Gamma_{ph} = \Gamma_{LA} + \Gamma_{TA} + \Gamma_{LO} + \Gamma_{HP} + \Gamma_{Fr}$ where

Γ_{LA} , Γ_{TA} , Γ_{LO} , Γ_{HP} and Γ_{Fr} are the scattering rates associated with LA, TA, LO, HP and Fr. phonons.

The LA and TA phonon scattering rates are given by $\Gamma_{ac} = \frac{m^* \Xi_{ac}^2 k_B T}{\hbar^3 \rho c_{ac}^2}$, where Ξ_{ac} is the acoustic phonon (LA or TA) deformation potential and c_{ac} is the acoustic phonon speed.

The intervalley polar longitudinal optical (LO) and intravalley homopolar optical (HP) phonon scattering rates are given by $\Gamma_{op}(E) = \frac{m^* D_{op}^2}{2\hbar^2 \rho \omega_{op}} [N_{op} + (1 + N_{op}) \Theta(E - \hbar \omega_{op})]$,

where D_{op} is the optical deformation potential of the optical phonon (LO or HP) and $N_{op} = [\exp(\hbar \omega_{op} / k_B T) - 1]^{-1}$ is its Bose-Einstein distribution with ω_{op} its phonon energy. $\Theta(\dots)$ is the usual Heaviside function.

In the long wavelength limit, the intravalley polar longitudinal optical (Froehlich) phonons can couple with the electron gas and undergo screening. Thus, the Froehlich optical phonon emission (+) or absorption (-) rate is⁴:

$$\Gamma_{Fr}^{\pm}(E) = \frac{e^2 \omega_{Fr} m^*}{8\pi \hbar^2} \left(\frac{1}{2} \pm \frac{1}{2} + N_{Fr} \right) \int_{-\pi}^{\pi} d\theta \frac{1 - \frac{k'}{k} \cos \theta}{q} \left(\frac{1}{\epsilon_{ion}^{\infty} + \epsilon_{el}(q)} - \frac{1}{\epsilon_{ion}^0 + \epsilon_{el}(q)} \right) \text{erfc} \left(\frac{q\sigma}{2} \right)^2$$

where k is the initial state, k' is the final state given by $k' = \sqrt{k^2 \mp 2m^* \omega_{Fr} / \hbar}$, and $q = \sqrt{k^2 + k'^2 - 2kk' \cos \theta}$. Also, ϵ_{ion}^{∞} (ϵ_{ion}^0) is the ionic part of the optical (static) permittivity of MoS₂, erfc is the complementary error function and σ is the sheet thickness.. We assume the phonon dispersion for the LO phonons to be flat so that $\omega_{Fr} = \omega_{LO}$. Therefore, the Froehlich phonon scattering rate is:

$$\Gamma_{Fr}(E) = \Gamma_{Fr}^{-}(E) + \Theta(E - \hbar \omega_{Fr}) \Gamma_{Fr}^{+}(E).$$

Fig. S1a shows the intrinsic phonon-limited mobility μ_{ph} as a function of temperature at $n=10^{13} \text{ cm}^{-2}$, calculated using the parameters in Table S1. μ_{ph} decreases with temperature and reaches $\sim 420 \text{ cm}^2/\text{Vs}$ at 300 K which is the maximum room-temperature electron mobility if there is no scattering with CI and SO phonons and in good agreement with published results^{1,4}. Fig. S1b shows μ_{ph} as a function of carrier density at 300 K. As we increase n , μ_{ph} grows initially because of the screening of the Froehlich coupling reduces its contribution to the intrinsic phonon scattering rate. However, at higher n , the scattering rate increases because the Fermi level is at the higher energy states where there is greater optical phonon (LO, HP and Fr.) emission and the corresponding scattering rate increases.

Parameter	Numerical value
m^*	$0.48 m_0$
$\Xi_{LA} (\Xi_{TA})$	2.8 eV (1.6 eV)
$c_{LA} (c_{TA})$	6700 m/s (4200 m/s)
ρ	$3.1 \times 10^{-7} \text{ g/cm}^2$
σ	$4.41 \times 10^{-10} \text{ m}$
$D_{LO} (D_{HP})$	$2.6 \times 10^8 \text{ eV/cm} (4.1 \times 10^8 \text{ eV/cm})$
$\omega_{LO} (\omega_{HP})$	48 meV (50 meV)
$\epsilon_{ion}^0 (\epsilon_{ion}^\infty)$	$7.6 \epsilon_0 (7.0 \epsilon_0)$

Table S1. Parameters used for the intrinsic phonon scattering rates. The values are taken from Ref. 1, 6.

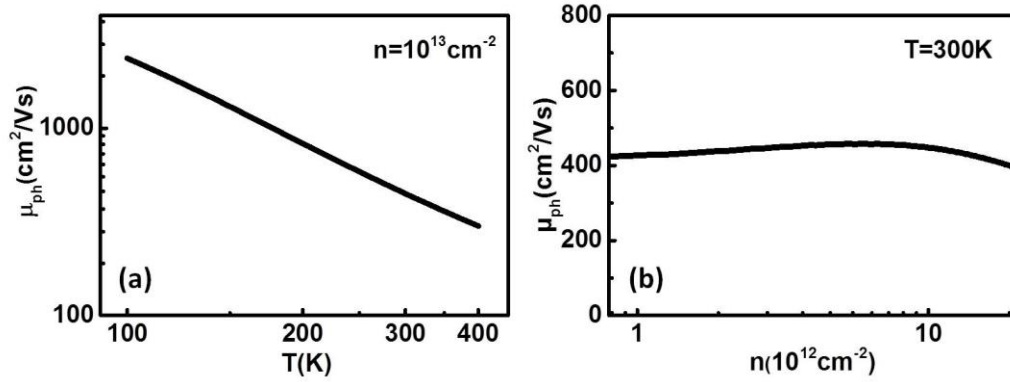


Figure S1. Theory for intrinsic phonon limited mobility. (a) μ_{ph} as a function of temperature at $n=1.0 \times 10^{13} \text{cm}^{-2}$. (b) μ_{ph} as a function of carrier density at $T=300\text{K}$.

c. Surface optical phonon scattering

Another source of electron scattering is through remote interaction with the polar optical phonons in the dielectric substrate^{4,7}. We assume that there are two phonon modes in SiO_2 and Al_2O_3 . The SO phonon scattering rate is given by $\Gamma_{SO} = \Gamma_{SO1} + \Gamma_{SO2}$. For HfO_2 , we assume that there is only one phonon mode though like in Ref.⁸.

The dielectric function of the substrate $\epsilon_{box}(\omega)$ is^{7, 9}:

$$\epsilon_{box}(\omega) = \epsilon_{box}^{\infty} + (\epsilon_{box}^i - \epsilon_{box}^{\infty}) \frac{\omega_{TO2}^2}{\omega_{TO2}^2 - \omega^2} + (\epsilon_{box}^0 - \epsilon_{box}^i) \frac{\omega_{TO1}^2}{\omega_{TO1}^2 - \omega^2} \quad \text{where } \epsilon_{box}^0, \epsilon_{box}^i \text{ and}$$

ϵ_{box}^{∞} are the static, intermediate and optical dielectric of the substrate, respectively, and

ω_{TO1} and ω_{TO2} are the transverse optical phonon angular frequencies such that

$\omega_{TO1} < \omega_{TO2}$. We can rewrite $\epsilon_{box}(\omega)$ in the generalized Lyddane-Sachs-Teller form

$$\epsilon_{box}(\omega) = \epsilon_{box}^{\infty} \left(\frac{\omega_{LO1}^2 - \omega^2}{\omega_{TO1}^2 - \omega^2} \right) \left(\frac{\omega_{LO2}^2 - \omega^2}{\omega_{TO2}^2 - \omega^2} \right). \text{ In the case of } \text{HfO}_2, \text{ we consider only one TO}$$

mode, so that its dielectric function is

$$\varepsilon_{box}(\omega) = \varepsilon_{box}^{\infty} + (\varepsilon_{box}^0 - \varepsilon_{box}^{\infty}) \frac{\omega_{TO}^2}{\omega_{TO}^2 - \omega^2} = \varepsilon_{box}^{\infty} \left(\frac{\omega_{LO}^2 - \omega^2}{\omega_{TO}^2 - \omega^2} \right) \quad \text{while} \quad \varepsilon_{tot,SO}^{\infty} = \frac{1}{2} (\varepsilon_{box}^{\infty} + \varepsilon_0)$$

and $\varepsilon_{tot,SO}^0 = \frac{1}{2} \left[\varepsilon_{box}^{\infty} \left(\frac{\omega_{LO}^2}{\omega_{TO}^2} \right) + \varepsilon_0 \right]$. The surface optical phonon frequencies (ω_{SO1} and ω_{SO2})

can be determined from the roots of the equation $\varepsilon_{box}(\omega) + \varepsilon_0 = 0$.

The remote interaction with the substrate SO phonons is described by the term

$$H_{SO} = \sum_{k,q} M_q c_{k+q}^{\dagger} c_k (a_q + a_{-q}) \quad \text{where } M_q \text{ is the coupling coefficient and } a_q^{\dagger} (a_q) \text{ is}$$

the phonon creation (annihilation) operator. The coupling coefficient is given by

$$M_q = \left[\frac{e^2 \hbar \omega_{SO}}{\Omega q} \left(\frac{1}{\varepsilon_{SO}^{\infty} + \varepsilon_{el}(q)} - \frac{1}{\varepsilon_{SO}^0 + \varepsilon_{el}(q)} \right) \right]^{1/2} \quad \text{where } \omega_{SO} \text{ is the SO phonon energy}$$

(Table 1). $\varepsilon_{SO}^{\infty}$ and ε_{SO}^0 are the optical and static dielectric response of the interface,

respectively. The term $\varepsilon_{el}(q)$ represents the screening effect of the electron gas on the

surface electric field of the substrate SO phonons and like in CI scattering, depends on the

temperature as well as the carrier density.

The remote optical phonon emission (+) and absorption (-) rates (SO1) can be written as

$$\Gamma_{SO1}^{\pm}(E) = \frac{e^2 \omega_{SO1} m^*}{8\pi \hbar^2} \left(\frac{1}{2} \pm \frac{1}{2} + N_{SO1} \right) \int_{-\pi}^{\pi} d\theta \frac{1 - \frac{k'}{k} \cos \theta}{q} \left(\frac{1}{\varepsilon_{tot,SO1}^{\infty} + \varepsilon_{el}(q)} - \frac{1}{\varepsilon_{tot,SO1}^0 + \varepsilon_{el}(q)} \right)$$

where $\varepsilon_{tot,SO1}^{\infty} = \frac{1}{2} \left[\varepsilon_{box}^{\infty} \left(\frac{\omega_{LO2}^2 - \omega_{SO1}^2}{\omega_{TO2}^2 - \omega_{SO1}^2} \right) + \varepsilon_0 \right]$ and

$$\varepsilon_{tot,SO1}^0 = \frac{1}{2} \left[\varepsilon_{box}^{\infty} \left(\frac{\omega_{LO1}^2}{\omega_{TO1}^2} \right) \left(\frac{\omega_{LO2}^2 - \omega_{SO1}^2}{\omega_{TO2}^2 - \omega_{SO1}^2} \right) + \varepsilon_0 \right]. \quad \text{Thus, the SO1 scattering rate is:}$$

$$\Gamma_{SO1}(E) = \Gamma_{SO1}^{-}(E) + \Theta(E - \hbar \omega_{SO1}) \Gamma_{SO1}^{+}(E). \quad \text{The SO2 scattering rate is similarly}$$

defined.

Figure S2 shows the SO phonon-limited mobility μ_{SO} calculated using Eq. (S1)

as a function of temperature at different values of n for SiO_2 , Al_2O_3 and HfO_2 . We observe that μ_{SO} increases with n because the remote interaction with the SO phonons undergoes greater screening at higher n like in CI scattering. Also, it decreases with temperature at a greater rate than μ_{ph} . Thus, at room temperature, it is one of the most dominant scattering processes especially for HfO_2 .

	SiO_2	Al_2O_3	HfO_2	Al_2O_3 (ref.)	HfO_2 (ref.)
ω_{TO1} (meV)	55.60	48.18	40.0	48.18	40.0
ω_{TO2} (meV)	138.10	71.41	-	71.41	-
ω_{LO1} (meV)	62.57	56.47	79.00	56.47	79.0
ω_{LO2} (meV)	153.28	120.55	-	120.55	-
ω_{SO1} (meV)	60.99	56.00	73.17	-	-
ω_{SO2} (meV)	148.87	108.00	-	-	-
ε_{box}^0 (ε_0)	3.90	10.00	16.50	12.53	16.00
ε_{box}^i (ε_0)	3.05	5.80	-	7.27	-
ε_{box}^∞ (ε_0)	2.50	2.56	4.23	3.20	4.10

Table S2. Parameters used for the SO phonon scattering rates. The values for SiO_2 and Al_2O_3 (ref.) are taken from Ref. 3; the values for HfO_2 (ref.) are taken from Ref. 8. ε_{box}^0 (or κ) for Al_2O_3 and HfO_2 are extracted from our capacitance measurements. The other parameters (ε_{box}^i and ε_{box}^∞) for Al_2O_3 and HfO_2 are obtained by rescaling the values for Al_2O_3 (ref.) and HfO_2 (ref.).

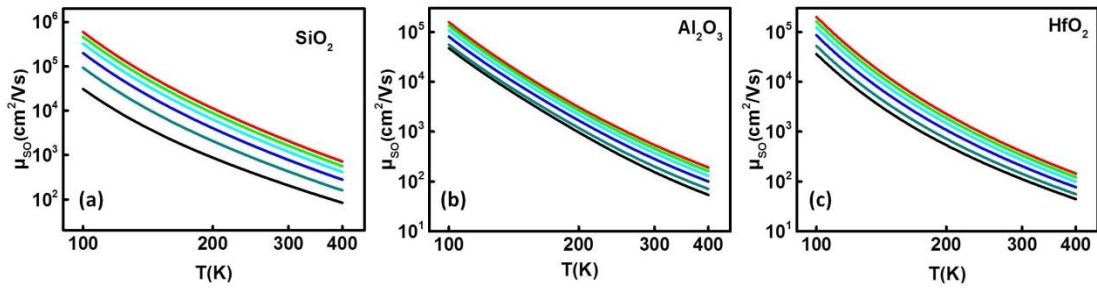


Figure S2. Theory for surface optical phonon limited mobility for different substrates. From top to bottom, $n=1.0 \times 10^{13} \text{ cm}^{-2}$ (red), $8 \times 10^{12} \text{ cm}^{-2}$ (green), $6 \times 10^{12} \text{ cm}^{-2}$ (cyan), $4 \times 10^{12} \text{ cm}^{-2}$ (blue), $2 \times 10^{12} \text{ cm}^{-2}$ (dark cyan) and $1 \times 10^{12} \text{ cm}^{-2}$ (black).

2. Growth and characterizations of high- κ oxides

We grew 10nm thick high- κ oxide on SiO_2/Si substrate by Atomic Layer Deposition (ALD). Before ALD, the substrate was thoroughly cleaned by acetone and isopropanol. For Al_2O_3 , trimethylaluminum (TMA, Micro-nano Tech. Co. Ltd., China) and H_2O were used as precursors. For HfO_2 , tetrakis(dimethylamido)hafnium (TDMAH, Micro-nano Tech. Co. Ltd., China) and H_2O were used as precursors. The deposition temperature was maintained at 150°C for both oxides.

We characterized the oxide films by surface roughness and dielectric constant measurements. The average mean-square roughness (R_q) calculated by AFM images is less than 0.2nm (Fig. S3a, b), similar to the SiO_2 substrate (Fig. S3c). This confirms the highly uniform and smooth surface of high- κ oxides, which is important for low CI. We measured the dielectric constant of the oxides by standard capacitance measurement with Au/oxide/Au structure using the Agilent E4980A precision LCR meter. The thickness of the

oxides is $\sim 100\text{nm}$ as obtained by AFM. We used the capacitance value at 10kHz, due to the negligible change of capacitance in low frequency regime.

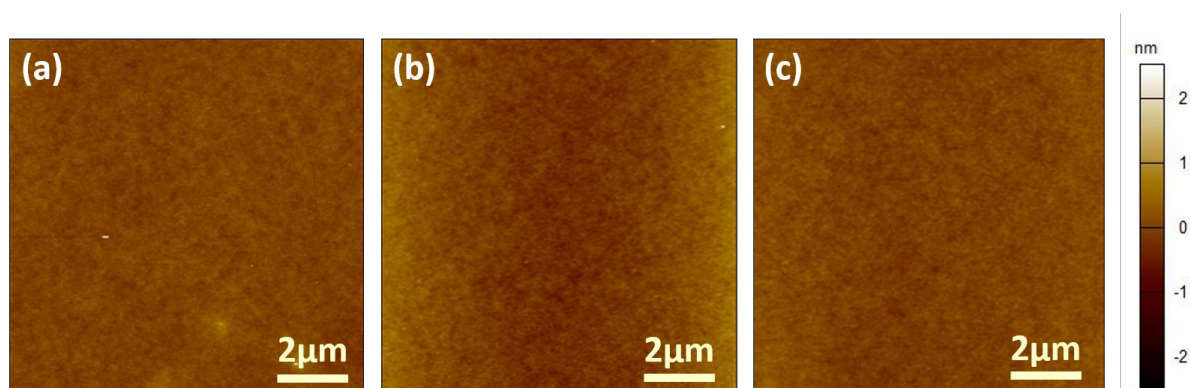


Figure S3. AFM characterization of high- κ oxide films. AFM images of (a) Al_2O_3 on SiO_2 , (b) HfO_2 on SiO_2 and (c) bare SiO_2 . The images all have the same Z scale.

3. Sample preparation, device fabrication and electrical measurements

We used the double-side MPS treatment reported in Ref. 10 for all samples studied here. Briefly, the 10nm high- κ oxide/285nm SiO_2/Si substrate was first subjected to a 30-min UV/ozone treatment to hydroxylate the oxide surface. The substrate was then dipped in a 10% (v/v) MPS/dichloromethane solution for 12 h in a dry glove box to grow MPS self-assembled monolayer. When MPS growth was finished, the substrate was sonicated in dichloromethane followed by thorough rinsing with dichloromethane and IPA, and drying with N_2 . We then exfoliated monolayer MoS_2 from natural flakes (SPI Supplies) on the MPS-treated substrate. After exfoliation, the sample was dipped in a fresh solution of 1/15 (v/v) MPS/dichloromethane for 24 h in a dry glove box to grow MPS on the top side of MoS_2 ,

followed by thorough rinsing. Finally, the sample was annealed in a mixture of H_2/Ar at $350\text{ }^\circ C$ for 20 min to finish the MPS treatment.

The source, drain and voltage probe electrodes of the field-effect transistors were then patterned by standard electron beam lithography, followed by electron beam evaporation of Ti/Pd (20nm/20nm) and lift-off. In the ebeam lithography step, we use double layer resist stack (MMA/PMMA), to reduce the exposure dose and form the undercut geometry. The devices were then annealed at $350^\circ C$ in Ar atmosphere for half an hour to improve contacts. Transport measurements were performed by a Keithley 4200 semiconductor parameter analyzer in a close-cycle cryogenic probe station with base pressure $\sim 10^{-5}$ Torr. 350K in situ vacuum annealing was performed to remove adsorbates and improve device performances before measurement¹¹.

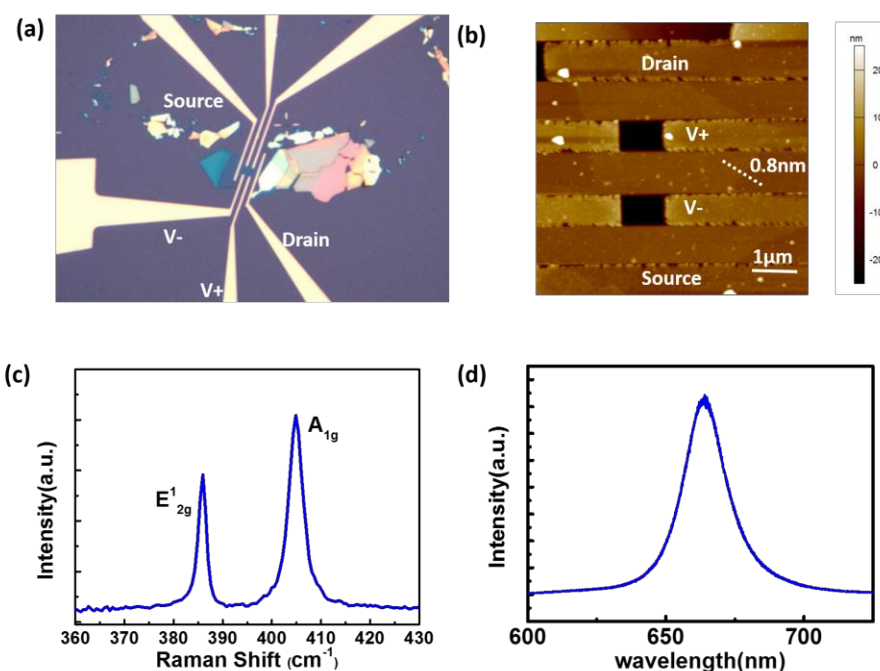


Figure S4. (a) Optical image of monolayer MoS₂ devices. (b) AFM image of monolayer MoS₂ device with height of 0.8 nm. (c) Raman spectrum of monolayer MoS₂ at 514.5 nm excitation.

The spectrum is shown with a distance of 19 cm^{-1} between two vibrating modes (E_{1g} and A_{1g})¹². (d) PL characterizations of monolayer MoS_2 .

4. Additional electrical data of devices on Al_2O_3 and HfO_2 substrate

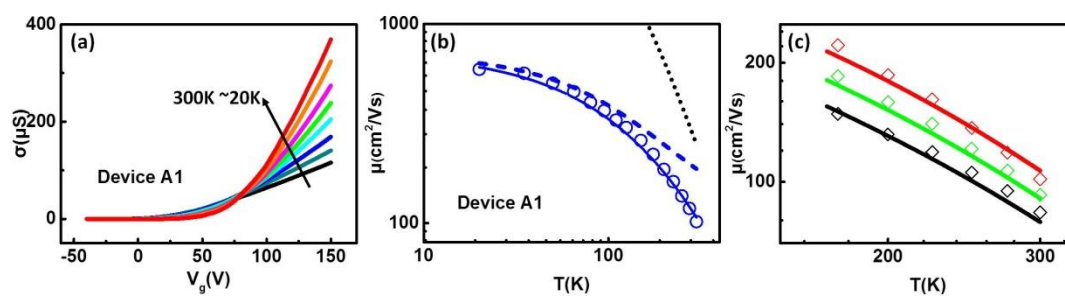


Figure S5. Electrical data and theoretical modeling for device A1 on Al_2O_3 substrate. (a) Four-probe conductivity as a function of V_g from 300K to 20K. (b) Field-effect mobility as a function of temperature under $n=1.0\times 10^{13}\text{ cm}^{-2}$ (symbols). The solid line is the best theoretical fitting (see Table 1 for fitting parameters). The blue dash line is calculated CI-limited mobility. The black dot line is the calculated phonon-limited mobility. (c) Field-effect mobility as a function of temperature at different carrier densities. The solid lines are the calculated results using parameters in Table 1. From top to bottom, $n=1.0\times 10^{13}\text{ cm}^{-2}$ (red), $8.5\times 10^{12}\text{ cm}^{-2}$ (green) and $7.0\times 10^{12}\text{ cm}^{-2}$ (black).

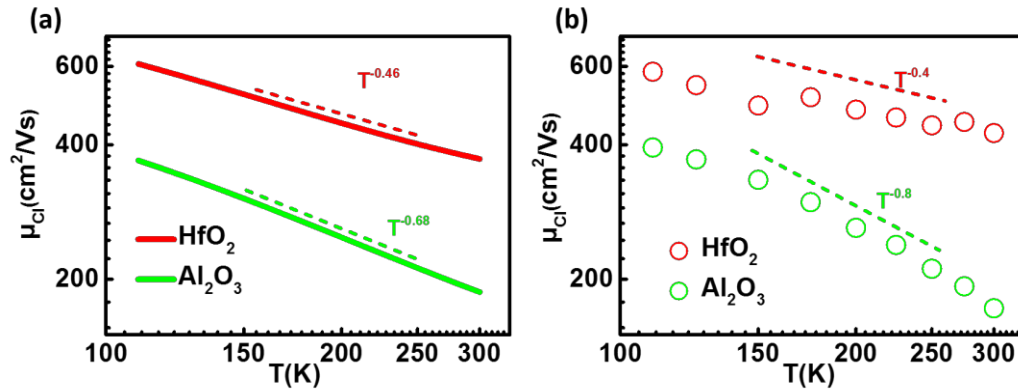


Figure S6. Theoretical (a) and experimental (b) μ_{Cl} as a function of temperature under $n=1.05 \times 10^{13} \text{cm}^{-2}$. The dash lines show T^γ scaling. Theoretically, the μ_{Cl} can be fitted by T^γ , where γ is an intrinsic parameter that reflects the dielectric screening. γ decreases as dielectric constant increases, $\gamma=0.46$ for HfO_2 and $\gamma=0.68$ for Al_2O_3 . The experimental data follow the same trend as theoretical predictions. The best power law fitting gives $\gamma=0.4$ for HfO_2 and $\gamma=0.8$ for Al_2O_3 , in reasonable agreement with our simulations.

References:

1. K. Kaasbjerg, K. S. Thygesen and K. W. Jacobsen, *Phys. Rev. B* **85** (11), 115317 (2012).
2. J. H. Davies, *The physics of low-dimensional semiconductors: an introduction*. (Cambridge University Press, Cambridge, UK, 1997).
3. Z.-Y. Ong and M. V. Fischetti, *Phys. Rev. B* **88** (16), 165316 (2013).
4. N. Ma and D. Jena, *Phys. Rev. X* **4** (1), 011043 (2014).
5. P. F. Maldague, *Surface Science* **73** (0), 296-302 (1978).
6. S. Kim, A. Konar, W.-S. Hwang, J. H. Lee, J. Lee, J. Yang, C. Jung, H. Kim, J.-B. Yoo, J.-Y. Choi, Y. W. Jin, S. Y. Lee, D. Jena, W. Choi and K. Kim, *Nat. Commun.* **3**, 1011 (2012).
7. Z.-Y. Ong and M. V. Fischetti, *Phys. Rev. B* **86** (16), 165422 (2012).

8. K. Zou, X. Hong, D. Keefer and J. Zhu, *Phys. Rev. Lett.* **105** (12), 126601 (2010).
9. M. V. Fischetti, D. A. Neumayer and E. A. Cartier, *J. Appl. Phys.* **90** (9), 4587-4608 (2001).
10. Z. Yu, Y. Pan, Y. Shen, Z. Wang, Z.-Y. Ong, T. Xu, R. Xin, L. Pan, B. Wang, L. Sun, J. Wang, G. Zhang, Y. W. Zhang, Y. Shi and X. Wang, *Nat. Commun.* **5** (2014).
11. H. Qiu, L. Pan, Z. Yao, J. Li, Y. Shi and X. Wang, *Appl. Phys. Lett.* **100**, 123104 (2012).
12. C. Lee, H. Yan, L. E. Brus, T. F. Heinz, J. Hone, and S. Ryu. *ACS Nano*, **4**, 2695, (2010).